Important Notice to Authors

Attached is a PDF proof of your forthcoming article in *Journal of Micro/Nanolithography, MEMS, and MOEMS*.

No further publication processing will occur until we receive your response to this proof. Please respond within 48 hours of receipt of this message.

Questions & Comments to Address

Please see the back page of this PDF proof for an itemized list of questions and comments to be addressed. The numbers listed correspond to numbers in the margin of the proof pages pinpointing the source of the question and/or comment. The numbers will be removed from the margins prior to publication.

Other Items to Check

- Figures submitted electronically as separate files containing color usually appear in color in the online journal. However, all figures will appear as grayscale images in the printed journal unless the color figure authorization form has been received and you have agreed to pay the necessary charges. For figures that will be color online but grayscale in print, please ensure that the text and caption clearly describe the figure to readers who view it only in black and white.
- Please check your title, author list, and acknowledgments carefully for any omissions or errors. Also check all text, illustrations, captions, equations, tables, references, and author biographies thoroughly. If you are adding biographies, note that they should not exceed 75 words each. Authors are encouraged to upload photographs and update their online SPIE profile on our website at http://spie.org/app/profiles/default.aspx.
- Please proofread the article very carefully. This will be your only opportunity to provide corrections. Note that responsibility for detecting errors lies with the author.
- Please check that your figures are accurate and sized properly. Figure quality in this proof is representative of the quality to be used in the online journal. To achieve manageable file size for online delivery, some compression and downsampling of figures may have occurred. Fine details may have become somewhat fuzzy, especially in color figures. The print journal uses files of higher resolution and therefore details may be sharper in print.

Ways to Respond

- Web: If you accessed this proof online, follow the instructions on the web page to submit corrections.
- Email: Send corrections to spie-manager@luminad.com. Include the paper number for your article in the subject line.

Forms

The *Journal of Micro/Nanolithography, MEMS, and MOEMS* offers the option of open access publication for a flat fee of $960 ($660 for Letters). Open access papers will be published under a Creative Commons CC BY 4.0 license. Authors who do not pay for open access will be published under the standard SPIE Transfer of Copyright agreement.

- Pay the open access fee online at http://spie.org/publications/journals/pubcharges.
- If you haven't already, complete the appropriate publication license online by logging into your account at http://jm3.msubmit.net.

If You Need to Contact Us

You may send an email message to spie-manager@luminad.com. Please reference the paper number and the first author of your article in your subject line. We will respond to you via email as quickly as possible.

Mechanistic insights in Zr- and Hf-based molecular hybrid EUV photoresists

Lianjia Wu,[a] Milos Baljozovic,[b] Giuseppe Portale,[c] Dimitrios Kazazis,[b] Michaela Vockenhuber,[b] Thomas Jung,[b] Yasin Ekinci,[b] and Sonia Castellanos[a,*]
[a]Advanced Research Center for Nanolithography, Amsterdam, The Netherlands
[b]Paul Scherrer Institute, Villigen, Switzerland
[c]University of Groningen, Zernike Institute of Advanced Materials, Groningen, The Netherlands

Abstract

Background. Inorganic resists show promising performances in EUV lithography. Yet, there is a need for understanding the exact chemical mechanisms induced by EUV light on these materials.

Aim. To gain knowledge on the EUV chemistry of inorganic resists, we investigate hybrid inorganic–organic molecular compounds, metal oxoclusters (MOCs). Their molecular nature allows for the monitoring of specific structural changes by means of spectroscopy and thus for the elucidation of the mechanisms behind pattern formation.

Approach. We compare the sensitivity of MOCs based on Zr and Hf, and methacrylate ligands as EUV resists. The chemical and structural changes causing the solubility switch were investigated by *ex situ* x-ray spectroscopy, infrared spectroscopy, ultraviolet–visible spectroscopy, and grazing incidence x-ray scattering.

Results. Higher sensitivity was detected for the Hf-based material, in line with its higher absorptivity. A small fraction of the carboxylate ligands is lost at doses that yield solubility contrast, whereas aggregation of the inorganic clusters was not observed.

Conclusions. These results provide evidence that, although the mechanism of solubility switch in these materials starts with decarboxylation reactions, it mainly proceeds through cross linking of the organic shells instead of aggregation of the inorganic clusters.

© 2019 Society of Photo-Optical Instrumentation Engineers (SPIE) [DOI: 10.1117/1.JMM.18.XX.XXXXXX]

Keywords: chemistry; spectroscopy; materials; metal oxocluster; inorganic resist.

Paper 18148 received Dec. 19, 2018; accepted for publication Feb. 11, 2019.

1 Introduction

With EUV lithography technology almost ready to be launched for high-volume manufacturing, there are still only few photoresists with the required performance for an optimal industrial throughput at the targeted 10-nm feature size.[1–4] Ideally, a photoresist should render patterns with line width roughness (LWR) below 20%.[4–6] Reaching this LWR limit, however, usually requires a dose high enough to keep the shot noise at an acceptable level. At the same time, the dose should be low enough (typically defined below 20 mJ/cm^2)[4–6] so that the exposure times allow for a high volume throughput.

Photoresists combining metallic elements and organic moieties are emerging as the most promising candidates for the next generation of photoresists.[1,3] It is generally accepted that the metallic atoms absorb a large fraction of the EUV light[7,8] while reactions of the organic parts are responsible for the solubility switching properties.[9–12] A particular mechanism that illustrates this distinction of the roles of organic and inorganic components in hybrid photoresists was proposed for the well-known Inpria type of non-chemically amplified resists, where the insolubility of the exposed areas arise from ligand cleavage and inorganic core aggregation.[13] In addition, the inorganic components in the photoresist provide the final patterns with good mechanical and chemical stability.[14,15] However, in addition to the absorptivity, other properties arising from the metallic elements can also affect the EUV-induced reactivity and, therefore, the sensitivity of the photoresist. Further, photoelectron emission cross sections at 13.5 nm can be drastically different for distinct metallic elements, and thus the composition of the inorganic core determines the primary photoelectron yields.[16,17] Brainard's group reported a correlation between reduction potential of the central metal in oxalate complexes (Co, Fe, and Cr) and their sensitivity as a resist material,[12] noting that this series of metals exhibited similar EUV cross sections. Reports by Ober and Giannelis have shown that both Zr oxide and Hf oxide nanoparticles rendered similarly high sensitivity (in the presence of photoacid generators), even though Hf has a higher EUV cross section than Zr.[18,19] Further investigations found that the sensitivity of photoresists based on Hf oxide nanoparticles toward DUV and EUV correlated with the stability of the cluster–ligand bond.[9] Therefore, it is highly relevant to elucidate what are the exact structural changes occurring right after photon absorption, to determine how their efficiency correlates to their molecular composition. This information can ultimately be used to optimize the materials to render a maximum

*Address all correspondence to Sonia Castellanos, E-mail: s.castellanos@arcnl.nl

1932-5150/2019/$25.00 © 2019 SPIE

change in their solubility properties upon exposure, which allows for a selective dissolution of either the exposed (positive tone resist) or the unexposed parts (negative tone resist) during the development process.

In the present report, the EUV photochemistry of metal oxoclusters (MOCs) based on Zr and Hf and featuring carboxylate ligands was prepared as a molecular compound and studied in detail. MOCs comprise a well-defined number of metallic atoms, bridged by O atoms and OH groups in their inorganic cores in a particular fixed arrangement.[20,21] The number of carboxylate ligands that are coordinated to the metals is also well-defined. Thus metal oxoclusters exhibit a structure composed of inorganic core and organic shell, like some nanoparticles. Yet, nanoparticles are typically prepared by sol–gel reactions that yield a distribution of different sizes and shapes, whereas oxoclusters are isolated as single-size molecules packed in molecular crystals that form during equilibrium reactions occurring in anhydrous conditions.

The aim of this study is to compare the photoresist behavior of two molecular materials with analogous chemical composition (M_xL_{2x}, M = metal, L = ligand) but featuring different inorganic cores in terms of sensitivity and gain understanding in the chemical changes responsible for the solubility switch. The chemical changes before and after EUV exposures (performed in an EUV interference lithography tool) were inspected *ex situ* by FTIR, ultraviolet–visible (UV–vis) absorption spectroscopies, and x-ray spectroscopy (XPS). In addition, structural changes in the thin film before and after exposure, such as the interparticle distance, were monitored by grazing-incidence x-ray scattering (GIXS).

2 Materials and Methods

2.1 *Materials Preparation and Characterization*

Zr-based methacrylate MOC (ZrMc) is commercially available by Sigma-Aldrich. This compound consists of a core of six Zr atoms clustered through four bridging O atoms (μ_3-O), four OH groups (μ_3-OH) and through twelve carboxylate groups of methacrylate ligands, giving the molecular formula $Zr_6O_4(OH)_4Mc_{12}$ (Mc = methacrylate).[22]

Hf-based methacrylate MOC (HfMc) was synthesized following the protocol in the literature.[23] The product was identified as the hexameric oxocluster with formula $Hf_6O_4(OH)_4Mc_{12}(HOBu)$ (Mc = methacrylate, Bu = butyl) from PXRD, MS (calculated $m/z = 2298.08$ M; found $m/z = 2322.81$ $M + Na + 2H^+$), NMR, infrared (IR), and thermogravimetric analyses (TGA). However, differences in the crystalline packing were detected from batch-to-batch. It must be noticed that the crystalline packing of these molecular crystals can be greatly affected by the presence of occluded molecules, such as solvent or methacrylic acid, and that the butoxide ligand can be shifted by the neighboring monodentate carboxylate ligand.[23]

NMR analysis was carried out using a Bruker AV-400 NMR spectrometer. The TGA were performed using a NETZSCH thermogravimetric analyzer in an Al_2O_3 crucible. Heating was performed from 35°C to 800°C at 10 K/min in an 80%/20% N_2/O_2 atmosphere. IR of the powder samples was performed in a Bruker ALPHA FTIR spectrometer. Powder x-ray diffraction experiments were carried out in Bruker D2 PHASER.

2.2 *Film Deposition and Lithography Tests*

Thin films of ZrMc and HfMc were prepared by spin coating (2100 rpm, 1 min) a solution from chloroform, $CHCl_3$, and propylene glycol methyl ether acetate (9:1 v/v) (8.4 mg/mL). Postapplication baking for 30 s at 90°C was applied to remove the remaining solvent. Samples for FTIR spectroscopy were spin coated on double side polished Si-wafer (200 μm). Samples for UV–vis absorption spectroscopy were spin coated on quartz substrates. Samples for XPS analyses were spin coated on Cr/Au-coated (2 nm/18 nm) coverslips.

2.3 *EUV Exposure*

EUV exposures were carried out at the XIL-II beamline of the Swiss light source (SLS) synchrotron at the Paul Scherrer Institute (PSI) with EUV light at 13.5 nm.[24] For the open-frame experiments, 0.5×0.5 mm^2 or 1.7×1.7 mm^2 areas were exposed to EUV light through a square aperture. For the patterning experiments, a transmission mask was used providing line/space patterns with pitches of 100, 80, 60, and 44 nm. Chloroform was used as a developer.

2.4 *Postexposure Analysis*

FTIR spectroscopy of the thin films was performed in transmission mode under vacuum in a Bruker Vertex 80v spectrometer. UV–vis absorption spectroscopy was performed in a Shimadzu UV2600 spectrophotometer. XPS experiments were performed *ex situ* and immediately after EUV exposure at PSI in a SPECS Analyzer Phoibos 150, with monochromatic AlK_α source (energy of 1486.6 eV, power 200 W).

Atomic force microscopy (AFM) images were made using a Bruker Dimension Icon, using the PeakForce tapping (ScanAsysAir) mode. The raw images were corrected for nonlinearities using first- and second-order corrections and the film thickness was measured by comparing the height of the film with the height of the substrate. Scanning electron microscopy (SEM) imaging was performed using a FEI Verios 460 with a voltage of 1 kV.

Grazing incidence small angle x-ray scattering (GIXS) experiments were performed both at the beamline BM26B of the European Synchrotron Radiation Facility, Grenoble (France) and at the MINA beamline at the University of Groningen (the Netherlands). An x-ray beam of about 0.3×0.3 μm^2 with a wavelength of 0.1 nm was used at the ESRF. The GIXS patterns were acquired using a Frelon CCD detector with a pixel size 48×48 μm^2. The sample-to-detector distance was 173 cm. At the MINA beamline, the x-ray wavelength was 0.154 nm, the circular beam size was about 0.5 mm, and the sample-to-detector distance was 24 cm. The detector used was a VANTEC500 multiwire chamber with pixel size of 136×136 μm^2. Images are presented with respect to the vertical $[q_z = 2\pi/\lambda(\sin\alpha_i + \sin\alpha_f)]$ and horizontal $[q_y = 2\pi/\lambda(\cos\alpha_f \sin 2\theta_f)]$ scattering wavevector, where λ is the x-ray wavelength, $2\theta_f$ is the horizontal scattering angle, and α_i and α_f are the incident and vertically scattered angles.

3 Results and Discussion

3.1 *Lithographic Performance*

A critical aspect of pattern formation in inorganic photoresists with metal-oxo cores and organic shells composed of carboxylate ligands is irreversible aggregation/condensation or structural rearrangements[25] upon spin coating and postapplication bake.[26] Depending on the extent of these changes, the solubility of the unexposed film can be slightly or drastically decreased. It had been previously observed that upon redissolution of the film made of the commercial ZrMc material, the individual molecular cluster could not be recovered as such.[10] Furthermore, Matson et al.[26,27] found that the chemical stability of Hf-based oxoclusters with methacrylate ligands upon different postapplication baking conditions had an important effect in the solubility of the thin films prepared with this material. In this work, this material is evidenced to lose the extra carboxylic acid molecules upon deposition. Originally, those carboxylic acids are not covalently bonded to the inorganic core but are occluded in the crystalline sample.[28] Their presence in the crystalline powder sample can be detected and in the IR spectrum [Figs. 1(a) and 1(b), C═O stretching at 1697 cm^{-1} and broadband between 2770 and 3515 cm^{-1} due to O—H stretching of the carboxylic acid, marked with asterisk] and it is further supported by the mass ratio between combustible organics and incombustible inorganic residue found in the TGA. In light of these results, we tentatively assign the first weight loss step at 150°C and from 140°C to 200°C in the TGA curves to the evaporation/combustion of these weakly bonded acids in the crystalline powder. The original formulae of the powder samples can thus be estimated from TGA as ZrMc·3McOH (15% weight loss at 150°C, 37% residue; calculated 13%, 38%) and HfMc·2.5Mc (8% weigh loss 140°C to 200°C, 49% residue; calculated 9%, 51%). We hypothesize that these extra noncoordinated ligands might stabilize the cluster in solution and in the crystalline form and that their loss in the thin films might make the clusters more susceptible to hydrolysis and/or rearrangements.

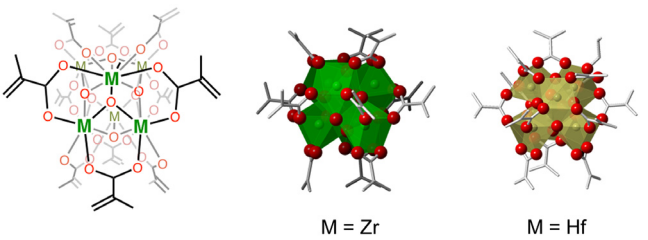

Fig. 1 Representation of metal oxoclusters used as photoresists in this work: (a) ZrMc and (b) HfMc. Polygons represent the coordination geometry, red spheres represent oxygen atoms and gray bars C—C bonds. Crystal structures from Refs. 23 and 29.

When comparing the IR spectra of the materials as powders and as thin films (Fig. 2), it was observed that the signals arising from extra free methacrylic acid (black asterisks) were barely detected, yet the broad peak from 2700 to 3700 cm^{-1} might arise from the O—H stretching mode of protonated carboxylic acid. The more defined band at 3670 cm^{-1} (red asterisk), on the other hand, is assigned to the O—H stretching of μ_3-OH groups bridging metallic atoms in the cluster.[30,31] It should be noticed that for HfMc this band was only detectable in the thin film. Nevertheless, this stretching mode can shift to lower wavenumbers when the OH group is involved in hydrogen bonding.[30]

The lithographic performance of ZrMc and HfMc was tested using synchrotron radiation at the SLS XIL-II end station.[24] The main goal was to compare the sensitivity of the two materials with analog structures and thus the same type of chemical bonding but based on different metals that have different 92-eV photon absorption cross sections. Since chloroform can dissolve the original bulk material, the solubility switch induced by EUV light was studied using chloroform as developer. Even if this might not be the optimal developer, using the same solvent for deposition and development, it gives direct evidence of chemical changes in the original material. HfMc displayed a lower dose-to-gel E_0 (<2 mJ/cm^2) than ZrMc (5 mJ/cm^2) as well as lower doses to attain the retainment of the whole resist thickness E_{100} [20 and 34 mJ/cm^2, respectively, Fig. 3(a)]. These trends in sensitivity follow the experimental linear absorptivity trends previously reported for these materials, that is, HfMc, having linear absorptivity $\mu = 9\ \mu m^{-1}$, needed less EUV photos to gel than ZrMc, with $\mu = 5\ \mu m^{-1}$.[32] The effect of thermal treatment was tested by heating the ZrMc sample to 100°C after exposure. However, postexposure baking did not affect the sensitivity of the ZrMc material thus indicating that no reactive intermediate species were formed after exposure [Fig. 3(b)].

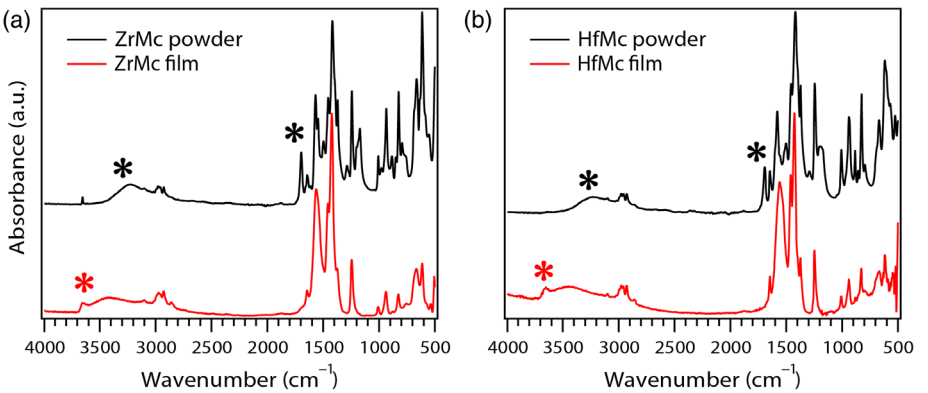

Fig. 2 IR spectra of (a) ZrMc and (b) HfMc as bulk powder (top, black) and thin film deposited on Si (bottom, red).

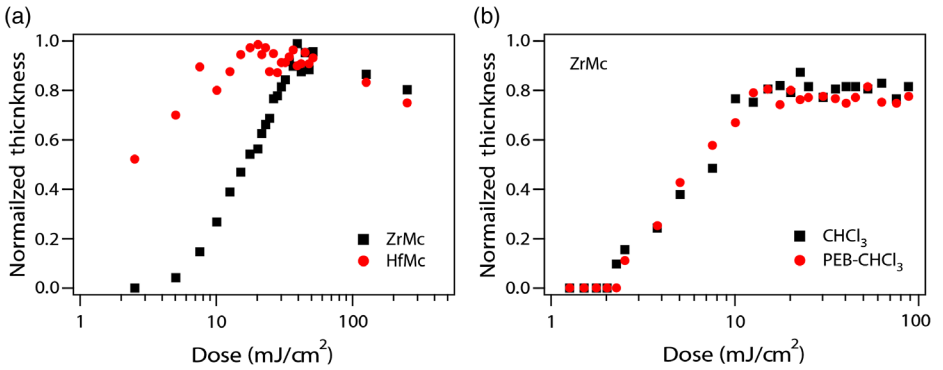

Fig. 3 (a) Contrast curve of ZrMc and HfMc developed with chloroform and (b) contrast curve of ZrMc before and after PEB with two different organic developers ($CHCl_3$ and THF).

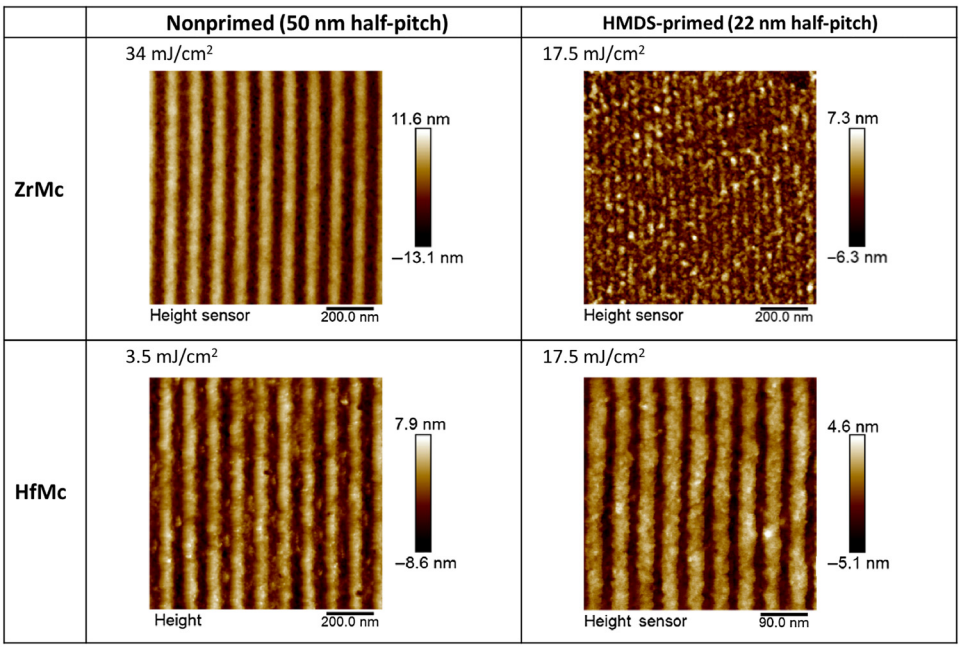

Fig. 4 AFM images of dense line patterns on ZrMc and HfMc.

The trends in sensitivity were also in agreement with the dose thresholds to pattern dense lines (Fig. 4). Formation of 50-nm half-pitch lines could be detected on HfMc at doses as low as 3.5 mJ/cm^2, indicating that a chemical change was promoted with EUV exposure. Nevertheless, low-solubility contrast together with scumming did not allow to resolve lines at higher doses. Priming the Si-substrates with hexamethyldiasilazane (HMDS) improved the development of patterns and smaller critical dimensions could be printed (22-nm half pitch).

SEM pictures confirmed that the unexposed material between the exposed lines remains after development for both investigated materials [Figs. 5(a)–5(c)]. In the case of HfMc, the detachment of large patches of resist was observed after exposure and development [Fig. 5(c)]. We suspect that the material changes its structure during the deposition (see Sec. 3.2) process, leading to interparticle bridging and the formation of aggregates. This causes a decrease in the solubility of the deposited thin film in $CHCl_3$. Furthermore, partial hydrolysis during or after deposition can result in strong interactions with the hydrophilic native oxide layer of the Si-wafer. This would explain the effect of HMDS: while aggregates might still form, the weaker interaction of the (partially hydrolized) clusters with the hydrophobic surface can result in the detachment of big areas during the development process.

Furthermore, the higher sensitivity of HfMc is accompanied by abundant bridging at low doses [Figs. 5(d) and 5(e)] and to a wide broadening [Fig. 5(f)] and an eventual merging of lines (not shown) that was not observed in the less sensitive material ZrMc. A potential explanation is given in Sec. 3.2.

3.2 *Origin of the Solubility Switch*

The chemical composition of the materials before and after exposure was investigated by XPS, FTIR, and UV–vis spectroscopy. The aim was to compare the reactivity of the ZrMc and HfMc materials and relate it to the threshold of photoconversion that renders a solubility change.

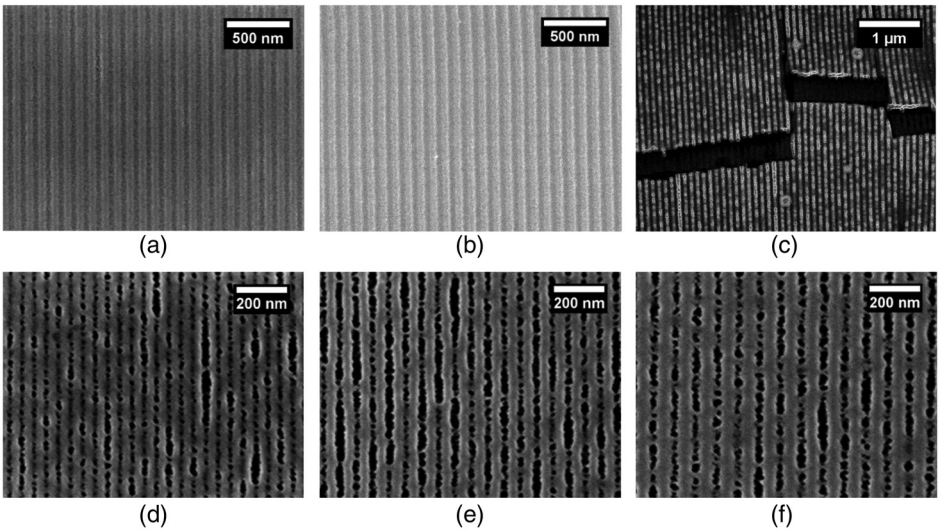

Fig. 5 SEM images of dense patterns printed with interference lithography. On top, 100 pitch patterns on (a) ZrMc at dose 57 mJ/cm^2, (b) ZrMc at 106 mJ/cm^2, and (c) HfMc (HMDS primed Si) at 20 mJ/cm^2. On bottom, patterns on HfMc (HMDS primed Si) with (d) 22 nm at 18 mJ/cm^2, (e) 30 nm at 21 mJ/cm^2, and (f) 40 nm half pitch at 22 mJ/cm^2.

The metal/O/C elemental ratio for the unexposed films of ZrMc and HfMc was lower than expected (estimated 1:5.3:8, found 1:3:7 in both materials). This ratio might be attributed to a loss of carboxylic ligands upon deposition (ca., 1.5 out of 12). It is likely that part of the carboxylate ligands rearranges to form intermolecular bridges between the clusters. For instance, the estimated ratio would match structures, in which three ligands are shared between two clusters in average. Such arrangements had been observed in crystalline structures of this type of compounds.[29,33] Furthermore, previous studies by Ober et al. showed that ZrMc material after deposition cannot be recovered as a discrete molecule. Recently, Mattson et al. proposed that rearrangements of the carboxylate ligands in Hf-based clusters as well as condensation reactions between the inorganic cores lead to solubility changes of the deposited materials compared to the bulk powder.[10,26,27] Yet, it should be noted that XPS probes the surface of the film and the ligand loss might be less in the bulk of the layer.

Inspection of the XPS high-resolution spectra for O 1s allows estimating the degree of decarboxylation at the dose where solubility switch occurs. The proposed fitting (Fig. 6) is based on three components assigned to COO (532 eV), Zr-O, such as μ_3-O groups (530 eV) and to Zr-OH (533 eV).[34] The estimated contribution of the oxygens in the carboxylate group (COO) in the O 1s peak before and after irradiation is shown in Fig. 7. A partial decarboxylation was observed, in line with previously reported studies,[10] whereas a rise in the concentration of Zr-OH species was observed. It should be noted that the cluster may hydrate after exposure due to adsorption of moisture from the air, since these are *ex situ* experiments.

Considering that the initial ZrMc material in the thin film contains a maximum of 12 carboxylate ligands per cluster, this would mean a maximum loss of around 1.4 carboxylate groups per cluster on average after 50 mJ/cm^2. The experimental EUV linear absorptivity of this material (5 μm^{-1})[7] implies that the transmittance of the 15-nm layer used for XPS is 93%. GIXS experiments (see below) reveal that the film is still formed of clusters arranged in a disordered manner with interparticle distances similar to the crystalline packing. The number of clusters in a volume of 15 nm $\times$ 1 cm^2 can thus be estimated from the cluster size and crystalline density so that an average of 0.2 absorbed photon per cluster is approximated at 50 mJ/cm^2 (1 of every 5 oxoclusters). With this assumption, a rough estimate would be that a maximum of seven carboxylate ligands is lost over five oxoclusters per absorbed photon at 50 mJ/cm^2, a dose sufficient to induce the solubility change in ZrMc. In the case of HfMc (9 μm^{-1}, T = 87%), only the sample at 250 mJ/cm^2 was available for analysis. At this dose, a 19% loss of the carboxylate groups was detected. Although these numbers are rough approximations, they indicate that the degree of ligand loss is not large at doses where the solubility switch occurs.

FTIR spectra of ZrMc and HfMc exposed materials revealed the partial bleach of the peaks attributed to the COO group stretching modes (Fig. 8). Two types of carboxylate ligands can be distinguished in ZrMc and HfMc compounds: bridging ligands, where the COO group binds to two different metallic atoms and chelating ligands, where a COO group is bonded to only one metallic atom. The peaks in the region of the IR spectrum where the vibrations attributed to the chelating COO are expected (1495 and 1459 cm^{-1})[35] decreases at a faster rate than those in the region where the vibration modes of the bridging carboxylate ligands are detected (>1500 cm^{-1}). Such difference in the decrease rate is more pronounced in the case of HfMc. This trend has been reported for TiO_x, ZrO_x, and HfO_x photoresists upon DUV irradiation,[37] and a faster reaction of chelating carboxylate ligands was also proposed by Ober et al. from XPS analyses of ZrO_x EUV photoresists.[10]

A decrease in the bands assigned to the terminal methacrylate group of the ligand (υ C=C at 1643 cm^{-1} and υ_{as} C(CH$_3$)=CH$_2$ at 1246 cm^{-1}) was also detected along with the decarboxylation. The decarboxylation reaction must indeed generate an allyl unit, most likely a radical that could either outgas or react with the neighboring methylene

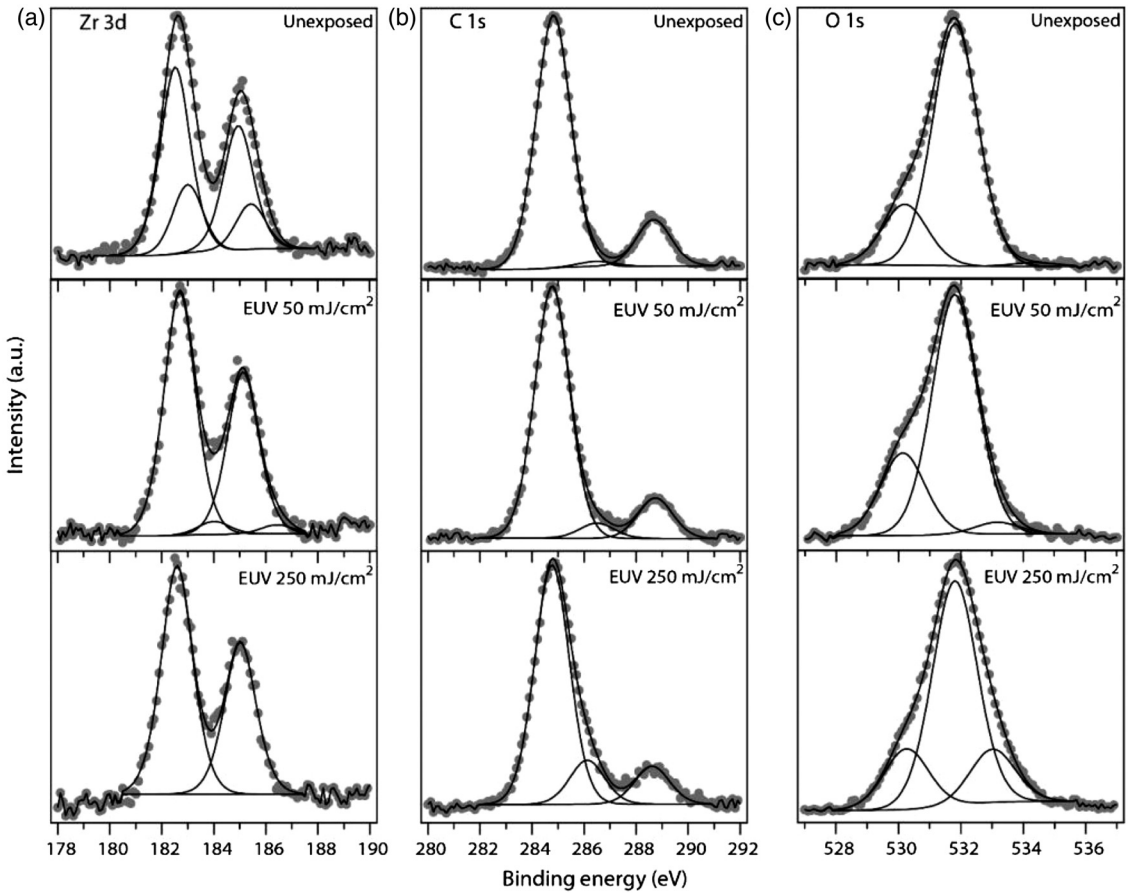

Fig. 6 High-resolution XPS spectra of (a) Zr 3d (b) C 1s and, and (c) O 1s of ZrMc before and after EUV exposure. Experimental data are shown as dots and fits as continuous lines.

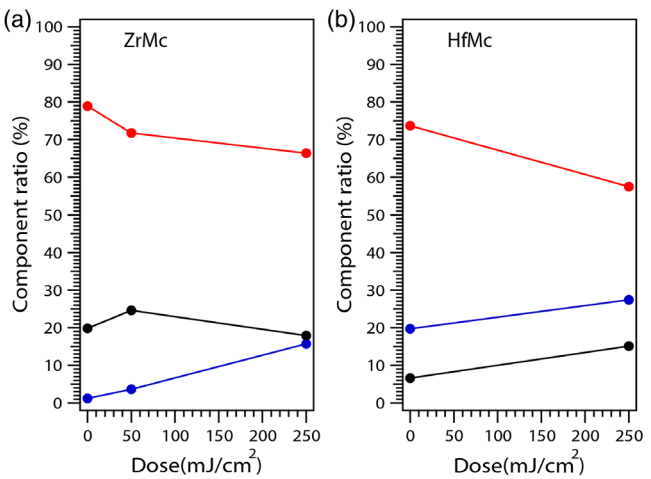

Fig. 7 The ratio of different components in the O 1s peak in XPS for (a) ZrMc and (b) HfMc changing with EUV doses, M–O (~530 eV) in black, COO (~532 eV) in red, and MOH (~533 eV) in blue.

terminal groups initiating a chain reaction and polymerization. The apparent relative increase of the C—H stretching is in agreement with such radical-induced reaction.

UV–vis absorption spectra (Fig. 9) are in line with the observed changes in XPS and IR spectroscopy. A bleach of the 220 nm, attributed to electronic transitions mainly located in the methacrylate ligands ($\pi^{®}\pi*$), is detected. This is an indication of the decrease of terminal double bonds, either due to outgassing or to their radical-induced reaction, which yields single carbon bonds.

In order to gain more insights into the solubility switch mechanism, the particle packing in the amorphous layer before and after EUV exposure was investigated in ZrMc by means of GIXS experiments. Given the marked difference in density between the carbon-based methacrylate shell and the metal oxide inorganic core, x-ray scattering experiments allow for the measurement of the average distance between the inorganic clusters. GIXS experiments were performed on thin films of the soluble material (unexposed) and on thin films of the insoluble material (samples exposed to 50 and 250 mJ/cm^2 and subsequently developed). The GIXS patterns in Figs. 10(a) and 10(b) exhibit a single-broad Debye–Scherrer like ring, suggesting that the thin-film structure consists of ZrMc clusters arranged in a 3-D disordered manner.[38] Nevertheless, the scattering ring shows some anisotropy suggesting a preferential packing in the direction parallel to the Si substrate, a common arrangement of disordered multilayered nanoparticles.[39] The average spacing among clusters along the q_y horizontal direction calculated according to the Bragg's law from the position of the scattering maxima in the intensity cuts reported in Fig. 10(d) was found to be $d = 2\pi/q_y^{\max} = 1.2$ nm for the unexposed ZrMc. These values are in agreement with the cluster packing obtained from XRD data.[29] After exposure, the scattering intensity related to the distance between neighboring clusters

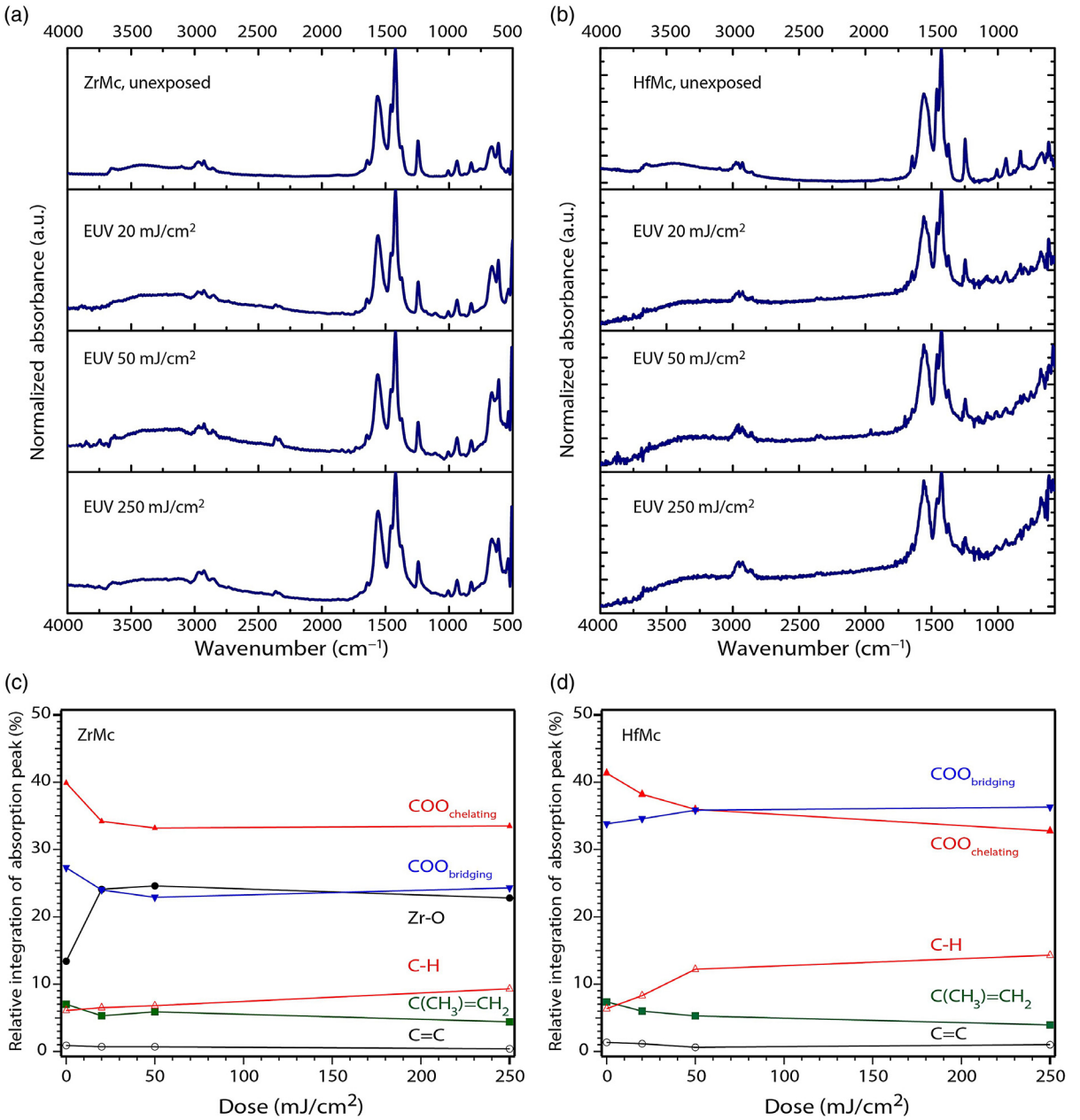

Fig. 8 Normalized FTIR spectra before and after exposure to different EUV doses of (a) ZrMc and (b) HfMc. Relative integration values (%) of FTIR peaks upon EUV exposure: υ_{as} Zr–O–Zr (714 to 644 cm^{-1}), υ_sC(CH$_3$)=CH$_2$ (1246 cm^{-1}), υ_s bridging COO + $\upsilon_{s/as}$ chelating COO (1334 to 1487 cm^{-1}), υ_{as} bridging COO (1488 to 1634 cm^{-1}), υC=C (1643 cm^{-1}).[30,35,36]

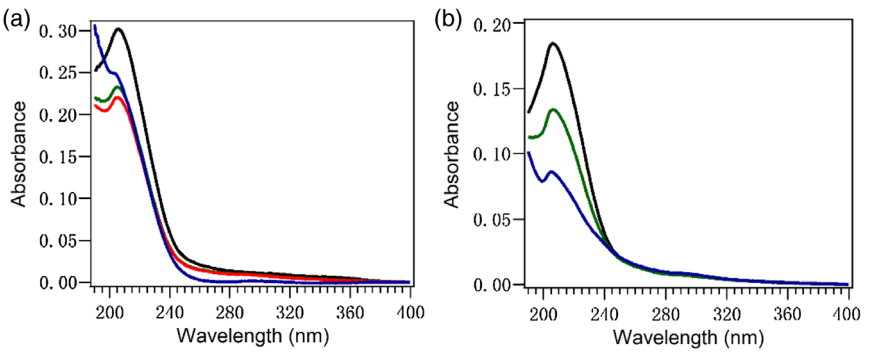

Fig. 9 UV–vis absorption spectra of (a) ZrMc and (b) HfMc before exposure (black) and after 20 mJ/cm^2 (green), 50 mJ/cm^2 (red), and 250 mJ/cm^2 (blue).

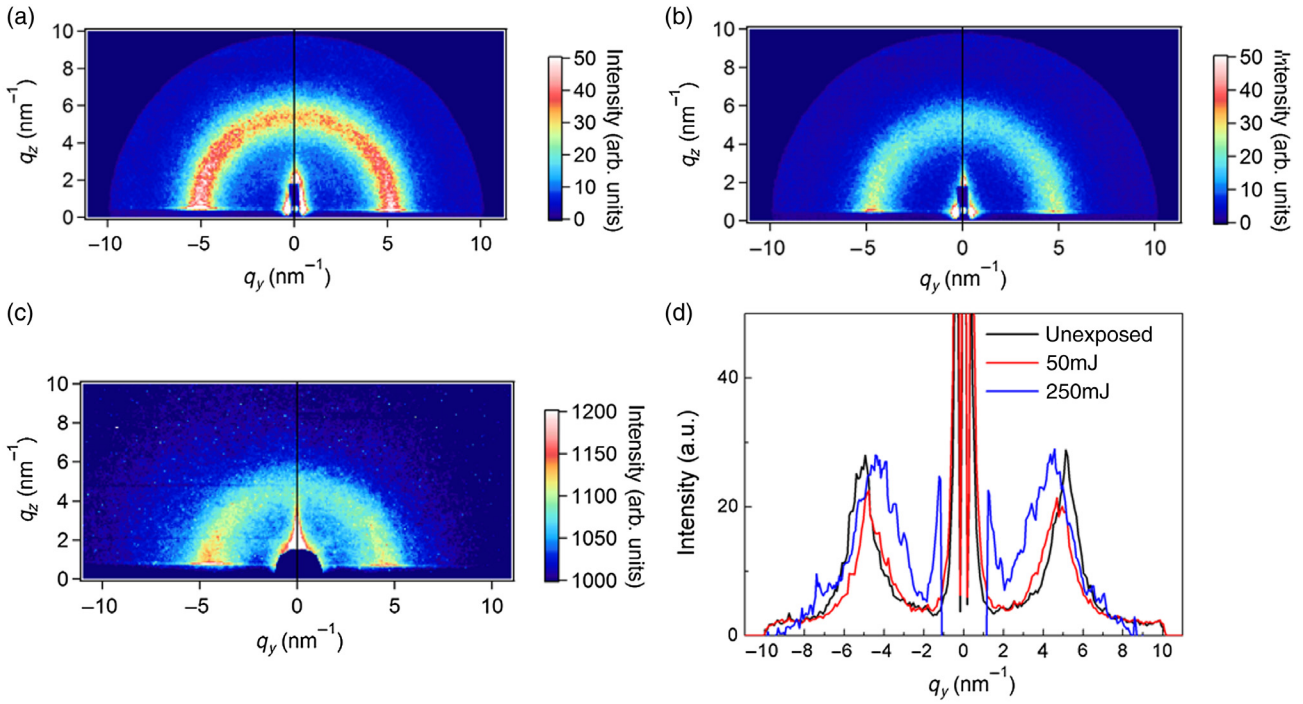

Fig. 10 GIXS results for thin films of ZrMc: (a) unexposed, (b) after 50 mJ/cm^2 exposure and development, (c) after 250 mJ/cm^2 exposure and development, and (d) comparison of the horizontal intensity cuts as a function of the exposure conditions. The intensity of the cuts has been normalized with respect to the exposure time and the actual sample dimension. For all the samples, the substrate is Si/SiO_2.

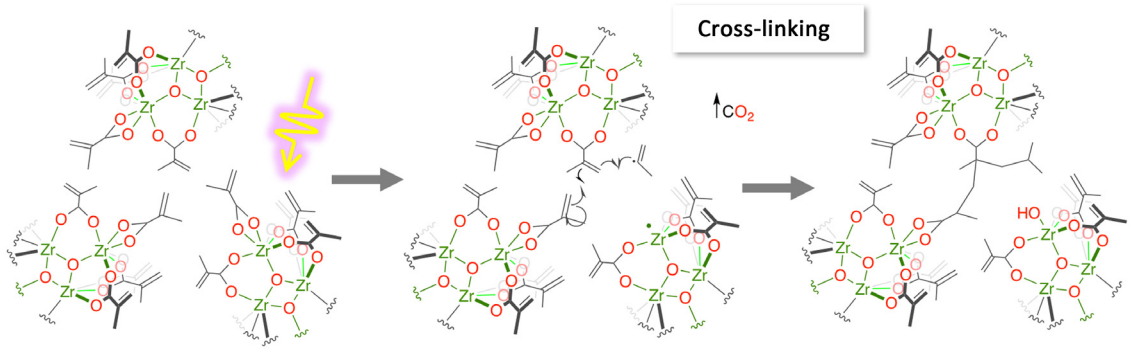

Fig. 11 Scheme of solubility change mechanism in MOCs featuring methacrylate ligands.

becomes weaker. The intensity decrease is mostly due to the smaller areas left after exposure and development of the samples. Indeed, after normalization for the actual sample dimension along the beam path, the unexposed and exposed samples show similar scattered intensity [Fig. 10(d)]. After the 50-mJ/cm^2 dose, a slight broadening and shift of the signal to $d = 1.4$ nm are detected. The broadening and shift are even more pronounced after 250-mJ/cm^2 dose. This trend is associated with an increase in the packing disorder of the particles, i.e., a wider distribution of interparticle distances, and to a small increase of the particle size. These minor changes for both the interparticle distance and peak width observed after 50 mJ/cm^2 indicate that the degree of aggregation is rather small, which is in line with the low shrinking observed at the dose-to-gel in the contrast curve of this material. It also supports the cross linking of the organic shells as an important part of the solubility switch mechanism.

Based on the spectroscopic and structural studies, we propose the mechanism shown in Fig. 11. Upon exposure, direct ionization by EUV photons and ionization during electron scattering lead to decarboxylation events and generation of allyl radicals. The latter initiate a chain reaction that cross links the molecular clusters (radical polymerization propagation), leading to a hybrid network that becomes insoluble in chloroform. We hypothesize that the higher absorption of HfMc might lead to a more efficient propagation of the reaction, which leads to a broadening (blur) of the patterned features already at relatively low doses, as discussed in Sec. 3.1.

4 Conclusions

Molecular hybrid materials known as metal oxoclusters based on Zr and Hf and methacrylate ligands were tested as EUV photoresists. Partial loss and rearrangement of carboxylate ligands in this type of compounds can affect the

solubility of the thin films after deposition and might be the cause of the scumming in the dense line patterns. These observations highlight the importance of the dynamic bonding between carboxylate binding groups and metal oxoclusters and demand the optimization of the clusters stability in thin films by molecular engineering, for instance, using more stable binding groups in the organic ligands. HfMc displayed higher sensitivity than ZrMc, thus following the trends in linear absorptivity. Although the structural changes upon EUV exposure for the two types of clusters were similar, a higher reactivity of chelating ligands was detected in HfMc, according to *ex situ* IR analyses of the thin films. The higher reactivity of HfMc compared to ZrMc is also accompanied by a much marked blur and bridging in the dense line patterns, which could arise from the propagation of cross linking to unexposed areas. X-ray photoelectron spectroscopy indicates that the loss of a small number of carboxylate groups (in the order of 12%) is sufficient to render the solubility switch in ZrMc. This low order of decarboxylation is accompanied by an increase of disorder in the packing of the solid film, which keeps the interparticle distance of the unexposed materials, according to GIXS experiments. These results manifest that the solubility switch in these materials does not result from a high degree of aggregation of the inorganic cores but arises from other structural rearrangements deriving from decarboxylation reactions, with a high contribution of cross linking of the terminal alkene groups in the organic ligands.

Acknowledgments

This project has received funding from the EU-H2020 research and innovation program under Grant Agreement No. 654360 having benefitted from the access provided by PSI in Villigen within the framework of the Nanoscience Foundries and Fine Analysis Europe Transnational Access Activity (NFFA projects ID234 and ID269). M. B. and T. A. J. acknowledge the Swiss National Science Foundation (Grant No. 200020-153549, 200020-175800 and 206021-113149). The authors thank R. Schelldorfer for technical support in the XPS and AFM measurements. S. C and L. W. thank the support in the synchrotron experiments of Yu Zhang. Parts of this work have been published as an SPIE Proceeding paper [S. Castellanos, L. Wu, M. Baljozovic, G. Portale, D. Kazazis, M. Vockenhuber, Y. Ekinci, T. Jung, Extreme Ultraviolet (EUV) Lithography IX, edited by Kenneth A. Goldberg, Vol. 10583, 105830A © 2018 SPIE]. The authors declare that they have no conflict interests regarding the publication of this article.

References

1. P. D. Ashby et al., "Resist materials for extreme ultraviolet lithography: toward low-cost single-digit-nanometer patterning," *Adv. Mater.* **27**, 5813–5819 (2015).
2. H. Nakagawa, T. Naruoka, and T. Nagai, "Recent EUV resists toward high volume manufacturing," *J. Photopolym. Sci. Technol.* **27**, 739–746 (2014).
3. L. Li et al., "Extreme ultraviolet resist materials for sub-7 nm patterning," *Chem. Soc. Rev.* **46**, 4855–4866 (2017).
4. O. Yildirim et al., "Improvements in resist performance towards EUV HVM," *Proc. SPIE* **10143**, 101430Q (2017).
5. D. De Simone et al., "EUV photoresist patterning characterization for imec N7/N5 technology," *Proc. SPIE* **10583**, 105830G (2018).
6. A. Lio, "EUV resists: what's next?" *Proc. SPIE* **9776**, 97760V (2016).
7. R. Fallica et al., "Absorption and exposure kinetics of photoresists at EUV," *Proc. SPIE* **10143**, 101430A (2017).
8. R. Fallica et al., "Dynamic absorption coefficients of chemically amplified resists and nonchemically amplified resists at extreme ultraviolet," *J. Micro/Nanolithogr. MEMS MOEMS* **15**, 033506 (2016).
9. L. Li et al., "Studying the mechanism of hybrid nanoparticle photoresists: effect of particle size on photopatterning," *Chem. Mater.* **27**, 5027–5031 (2015).
10. V. Kosma et al., "Elucidating the patterning mechanism of zirconium-based hybrid photoresists," *J. Micro/Nanolithogr. MEMS MOEMS* **16**, 041007 (2017).
11. Y. Zhang et al., "Photochemical conversion of tin-oxo cage compounds studied using hard x-ray photoelectron spectroscopy," *J. Micro/Nanolithogr. MEMS MOEMS* **16**, 023510 (2017).
12. S. Grzeskowiak et al., "Reactivity of metal-oxalate EUV resists as a function of the central metal," *Proc. SPIE* **10146**, 1014605 (2017).
13. W. D. Hinsberg and S. Meyers, "A numeric model for the imaging mechanism of metal oxide EUV resists," *Proc. SPIE* **10146**, 1014604 (2017).
14. M. Trikeriotis et al., "Nanoparticle photoresists from HfO_2 and ZrO_2 for EUV patterning," *J. Photopolym. Sci. Technol.* **25**, 583–586 (2012).
15. D. De Simone et al., "Demonstration of an N7 integrated fab process for metal oxide EUV photoresist," *Proc. SPIE* **9776**, 97760B (2016).
16. J. J. Yeh, *Atomic Calculation of Photoionization Cross-Sections and Asymmetry Parameters*, Gordon and Breach Science, Langhorne, Pennsylvania (1993).
17. Y. Vesters et al., "Sensitizers in EUV chemically amplified resist: mechanism of sensitivity improvement," *Proc. SPIE* **10583**, 1058307 (2018).
18. M. Kryask et al., "Nanoparticle photoresists: ligand exchange as a new, sensitive EUV patterning mechanism," *J. Photopolym. Sci. Technol.* **26**, 659–664 (2013).
19. C. Ober and E. Giannelis, "New oxide nanoparticle extreme-UV photoresists achieve high sensitivity," *SPIE Newsroom* 2–4 (2014).
20. U. Schubert, "Cluster-based inorganic–organic hybrid materials," *Chem. Soc. Rev.* **40**, 575–582 (2011).
21. H. Assi et al., "Titanium coordination compounds: from discrete metal complexes to metal-organic frameworks," *Chem. Soc. Rev.* **46**, 3431–3452 (2017).
22. G. Kickelbick and U. Schubert, "Oxozirconium methacrylate clusters: $Zr_6(OH)_4O_4(OMc)_{12}$ and $Zr_4O_2(OMc)_{12}$ (OMc = methacrylate)," *Chem. Ber.* **130**, 473–478 (1997).
23. S. Gross et al., "Mono-, di-, and trimetallic methacrylate-substituted metal oxide clusters derived from hafnium butoxide," *Monatsh. Chem.* **134**, 1053–1063 (2003).
24. N. Mojarad, J. Gobrecht, and Y. Ekinci, "Interference lithography at EUV and soft x-ray wavelengths: principles, methods, and applications," *Microelectron. Eng.* **143**, 55–63 (2015).
25. L. Li et al., "Solubility studies of inorganic-organic hybrid nanoparticle photoresists with different surface functional groups," *Nanoscale* **8**, 1338–1343 (2016).
26. E. C. Mattson et al., "Role of excess ligand and effect of thermal treatment in hybrid inorganic-organic EUV resists," *Proc. SPIE* **10583**, 1058309 (2018).
27. E. C. Mattson et al., "Chemical modification mechanisms in hybrid hafnium oxo-methacrylate nanocluster photoresists for extreme ultraviolet patterning," *Chem. Mater.* **30**, 6192–6206 (2018).
28. F. Faccioli et al., "Hydrolytic stability and hydrogen peroxide activation of zirconium-based oxoclusters," *Eur. J. Inorg. Chem.* **2015**, 210–225 (2015).
29. G. Kickelbick, P. Wiede, and U. Schubert, "Variations in capping the $Zr_6O_4(OH)_4$ cluster core: x-ray structure analyses of $[Zr_6(OH)_4O_4(OOC\text{-}CH\text{-}CH_2)_{10}]_2(\mu\text{-}OOC\text{-}CH\text{-}CH_2)_4$ and $Zr_6(OH)_4O_4(OOCR)_{12}(PrOH)$ (R = Ph, CMe = CH_2)," *Inorg. Chim. Acta* **284**, 1–7 (1999).
30. P. Piszczek et al., "The new type of $[Zr_6(\mu_3\text{-}O)_4(\mu_3\text{-}OH)_4]$ cluster core: crystal structure and spectral characterization of $[Zr_6O_4(OH)_4(OOCR)_{12}]$ (R = Bu^t, $C(CH_3)_2Et$)," *Polyhedron* **26**, 679–685 (2007).
31. V. Guillerm et al., "A zirconium methacrylate oxocluster as precursor for the low-temperature synthesis of porous zirconium(IV) dicarboxylates," *Chem. Commun.* **46**, 767–769 (2010).
32. R. Fallica et al., "Absorption coefficient of metal-containing photoresists in the extreme ultraviolet," *J. Micro/Nanolithogr. MEMS MOEMS* **17**, 023505 (2018).
33. M. Puchberger et al., "Can the Clusters $Zr_6O_4(OH)_4(OOCR)_{12}$ and $[Zr_6O_4(OH)_4(OOCR)_{12}]_2$ be converted into each other?" *Eur. J. Inorg. Chem.* **2006**, 3283–3293 (2006).
34. P. C. Wong et al., "XPS investigations of the interactions of hydrogen with thin films of zirconium oxide II. Effects of heating a 26 Å thick film after treatment with a hydrogen plasma," *Appl. Surf. Sci.* **89**, 263–269 (1995).
35. J. Kreutzer, P. Blaha, and U. Schubert, "Assessment of different basis sets and DFT functionals for the calculation of structural parameters, vibrational modes and ligand binding energies of

$Zr_4O_2(carboxylate)_{12}$ clusters," *Comput. Theor. Chem.* **1084**, 162–168 (2016).

36. J. Kreutzer et al., "Retention of the cluster core structure during ligand exchange reactions of carboxylato-substituted metal oxo clusters," *Eur. J. Inorg. Chem.* **2015**, 2145–2151 (2015).
37. F. Stehlin et al., "Room-temperature preparation of metal-oxide nanostructures by DUV lithography from metal-oxo clusters," *J. Mater. Chem. C* **2**, 277–285 (2014).
38. G. Portale et al., "Influence of metal–support interaction on the surface structure of gold nanoclusters deposited on native SiO_x/Si substrates," *Phys. Chem. Chem. Phys.* **16**, 6649–6656 (2014).
39. J. Toudert et al., "Using ion beams to tune the nanostructure and optical response of co-deposited Ag:BN thin films," *J. Phys. D Appl. Phys.* **40**, 4614–4620 (2007).

Biographies of the authors are not available.

Queries

1. Please provide expansion for the terms EUV, FTIR, PXRD, and MS at the first occurrence.

2. References (10 and 28) seem to be same. So, duplicate reference 28 has been deleted and further references are renumbered sequentially. Please check and confirm.

3. As per style, images are not allowed in the tables. Hence, Table 1 is treated as Fig. 4 and the remaining figures are renumbered sequentially both in the text and list. Please check.

4. Please provide volume number for Reference 19.

5. Please check and confirm the insertion of article title for Reference 23.

6. Please provide 75-word biographies of the authors, if available.

Funding Information

The authors have identified the following funders and award numbers, either on the submission form at the time of submission or in the Acknowledgments of the manuscript. Please check this list of funding agencies and make any necessary corrections using the full and official name of the funding organization. You may also wish to edit the Acknowledgments, if needed. This information may be used to help SPIE comply with funding reporting mandates.

- Horizon 2020 Framework Programme; Award no. 654360; Funder ID https://doi.org/10.13039/100010661
- Swiss National Science Foundation (Schweizerische Nationalfonds); Award no(s). 200020-153549, 200020-175800, 206021-113149; Funder ID https://doi.org/10.13039/501100001711